Eur. J. Mech. B - Fluids 19 (2000) 745–764

S0997-7546(00)00127-8/FLA

Boundary-layer investigations on a model of the ELAC 1 configuration at high Reynolds numbers in the DNW

Egon Krause *, Ronald Abstiens, Stefan Fühling, Vitali N. Vetlutsky

Aerodynamisches Institut, RWTH Aachen, Aachen, Germany

(Received 1 April 1999; revised and accepted 7 March 2000)

Abstract – Results of boundary-layer investigations on the leeward side of a 1: 12 scale model of the ELAC 1 configuration of a space transportation system are presented. The configuration has the shape of a thick delta wing with a rounded leading edge. The model length is 6 m; the experiments were carried out in the 8×6 m^2 low-speed German-Dutch-Windtunnel at Reynolds numbers up to $\mathrm{Re} = 40 \cdot 10^6$. In a first series of experiments mean velocity profiles were determined in the turbulent boundary layer on the leeward side of the model, with a single hot-wire probe in the plane of symmetry at four positions. Comparison calculations with a numerical solution of the boundary-layer equations showed good agreement up to angles of attack $\alpha = 10°$. In a second series of tests the laminar-turbulent transition of the flow and its separation near the rounded leading edge were investigated at three positions with multi-sensor hot-film arrays with 40, 56, and 96 elements. These measurements demonstrated that the flow near the rounded leading edge is markedly influenced by the nose radius. © 2000 Éditions scientifiques et médicales Elsevier SAS

hot-wire / hot-film measurements / high-Reynolds number flow

Nomenclature

b	span of model
c_p	pressure coefficient
d	diameter of hot wire
e_rms	power, based on root-mean square value of hot-film signals
E	voltage
f	frequency of hot-film signals
F	flatness of hot-film signals
l	length of hot wire
l_i, l	length of model, defined in *figure 1*
r	cylindrical coordinate
Re	Reynolds number
rms	root-mean square value of hot-wire signals
s	local semi span
Tu	turbulence level
U_∞, u_∞	free-stream velocity
U_δ, u_δ	velocity at the outer edge of the boundary layer

* Correspondence and reprints; e-mail: ek@aia.rwth-aachen.de

u^+	non-dimensionalized tangential velocity component in the boundary layer
u_τ	friction velocity
y	coordinate in the spanwise direction
x	coordinate in the streamwise direction
η, z	boundary-layer coordinates, normal to the surface
z^+	non-dimensionalized boundary-layer coordinate, normal to the surface
α	angle of attack
β	angle of side slip
Δ	Rotta–Clauser length
θ	meridional angle
ρ	fluid density
ξ, ζ	boundary-layer coordinates, tangential to the body surface
$X^2_{a,b}$	coherence of hot-film signals of neighboring sensors
$\Psi_{a,b}$	coherence coefficient of hot-film signals of neighboring sensors
$\Delta\Phi$	phase difference of hot- film signals of neighboring sensors

Abbreviations

ELAC	ELiptische Auftriebs(C)onfiguration
DFG	Deutsche Forschungsgemeinschaft
DLR	Deutsches Zentrum für Luft- und Raumfahrt
DNW	Deutch-Niederländischer Windkanal
RWTH	Rheinisch-Westfälische Technische Hochschule
SFB	Special Colaborative Research Center

1. Introduction

High-Reynolds-number flow research, particularly in low-speed aerodynamics is mandatory from the point of view of basic considerations, but difficult to conduct for many reasons. This discrepancy has led to numerous disasters, reported in the literature, the major cause being that it is almost impossible to forecast flow behavior at high Reynolds number from experimental data, that were measured at much lower values. Similar problems exist for numerical predictions. For three-dimensional flows, the Reynolds stresses are, in general, not known and their modeling is difficult. In addition, the influence of inadequate numerical resolution on the accuracy of the prediction can often not be estimated because of limited storage capacity.

Since an easy solution to this problem is not in sight, high-Reynolds number experiments were designed and carried out in recent years in exceptional cases, despite the high costs. With such experiments, it is expected to acquire sets of reliable data with which numerical predictions can be compared in the future. One of the first of such experiments, hereafter referred to as the first DNW experiment, was carried out in 1994. In that experiment, H.H. Fernholz, M. Nockemann, M. Schober, and the first author, measured mean velocity and Reynolds-stress profiles in the incompressible turbulent boundary layer with zero pressure gradient on the aerodynamically smooth sidewall of the German-Dutch windtunnel in the Netherlands [1]. The measurements

provided a complete set of data of the turbulent stresses for Reynolds numbers, based on the momentum thickness, up to $Re_{\delta 2} \leqslant 6 \times 10^4$. The accuracy of the measurements was secured by employing two different hot-wire probes, placed side by side in the experimental set up.

Because of the success of the first DNW experiment, J.C. Rotta and H.U. Meier [2] suggested a second high-Reynolds number experiment in 1995. They proposed to measure spatial correlations in addition to mean velocity profiles, again for the flow conditions of the first experiment, described in reference [1]. A special support for the hot-wire probes was designed, and a second DNW experiment was carried out, again successfully by H.-P. Kreplin, O. Merschat, and R. Abstiens in 1996 [3]. The hot-wire measurements yielded profiles of the space correlations for 12 positions reported in [3]. H.H. Fernholz was deeply involved in the preparatory discussions of the second DNW experiment and made many helpful suggestions.

While the second DNW experiment was under way, a third was prepared within the scope of the research program of the Special Collaborative Research Center (SFB 253) at the RWTH Aachen on the topic "Fundamentals of Design of Aerospace Planes", sponsored by the DFG. In conjunction with investigations of the low-speed characteristics of aerospace planes, which usually have delta wings with a small aspect ratio, the reviewers of the program argued, – among them H.H. Fernholz – that the available laboratory windtunnel facilities were too small to cope with the high-Reynolds number problem of the low-speed starting and landing phase. Until then the low-speed characteristics of the lifting body configuration under investigation, a slender delta wing with rounded leading edges, the ELAC 1 (ELliptische Auftriebs(C)konfiguration) had been investigated in several windtunnels. Relatively small steel and plastic models, 1 : 65 and 1 : 250 scale, were used in the tests at Aachen and Darmstadt University of Technology, and at the German Aerospace Center (DLR) in Braunschweig, Göttingen, and Köln. Since the Reynolds numbers of the tests were rather low – with the exception of that of the high-pressure tunnel in Göttingen – it was suggested to conduct a high-Reynolds number experiment. Because of the previous positive experience, it was proposed to carry it out again in the German-Dutch windtunnel. The primary objective of the experimental campaign to be set up was to study the influence of high-Reynolds numbers on the flow behavior at low speeds, in a special research program sponsored by the DFG. After careful preparation of the experiments and construction of the model, the experiments were carried out in the DNW within two weeks in the fall of 1997. They included measurements of surface pressure distributions, aerodynamic forces and moments, velocity distributions in the primary vortex with particle image velocimetry and laser-light sheet technique, velocity profiles and wall shear at selected positions in the boundary layer on the leeward side of the wing, the laminar-turbulent transition and of the separation region near the rounded leading edge with the multi-sensor hot-film and surface oil flow technique. The data was evaluated during the year 1998. The preliminary results were presented at the GAMM Annual Meeting 1998, by D. Jacob, G. Neuwerth, and U. Peiter in [4], and in [5], by R. Abstiens, S. Fühling, and V.N. Vetlusky in [6], and by L. Dieterle and U. Peiter in [7].

In the following sections, the details of the boundary-layer investigation will be reported. They include a brief description of the experimental facility and the model, the measurements of the velocity profiles with hot-wire anemometry at selected positions, the computation of the measured part of the boundary layer with a numerical solution, and the study of transition and separation near the rounded leading edge with the hot-film technique.

2. Test facility, model, and experimental techniques

2.1. Test facility and model

The test facility used for this experiment was the 8×6 m^2 closed test section of the DNW. During the tests, the velocity could be varied between 15 m/s and 100 m/s. The temperature in the test section was kept constant

within $\pm 0.5°$ C during the measuring period. Other characteristics of the tunnel were described by H.U. Meier, U. Michel, and H.P. Kreplin in [8]. For example, the maximum deviation of the static pressure in the streamwise direction was reported to be $\Delta c_p = \pm 0.002$ over a distance of about 12 m, and the free-stream turbulence level was measured at 40 m/s to be $Tu = 0.027\%$ within a frequency range of 0.15 Hz to 10 kHz.

The geometry of the windtunnel model of the ELAC 1 configuration is depicted in *figure 1*, taken from [4]. The model had an overall length of about 6 m, which corresponds to a scale of 1 : 12. Its weight was about 16 kN; it was supported by a rear sting and equipped with an internal six component strain gage balance.

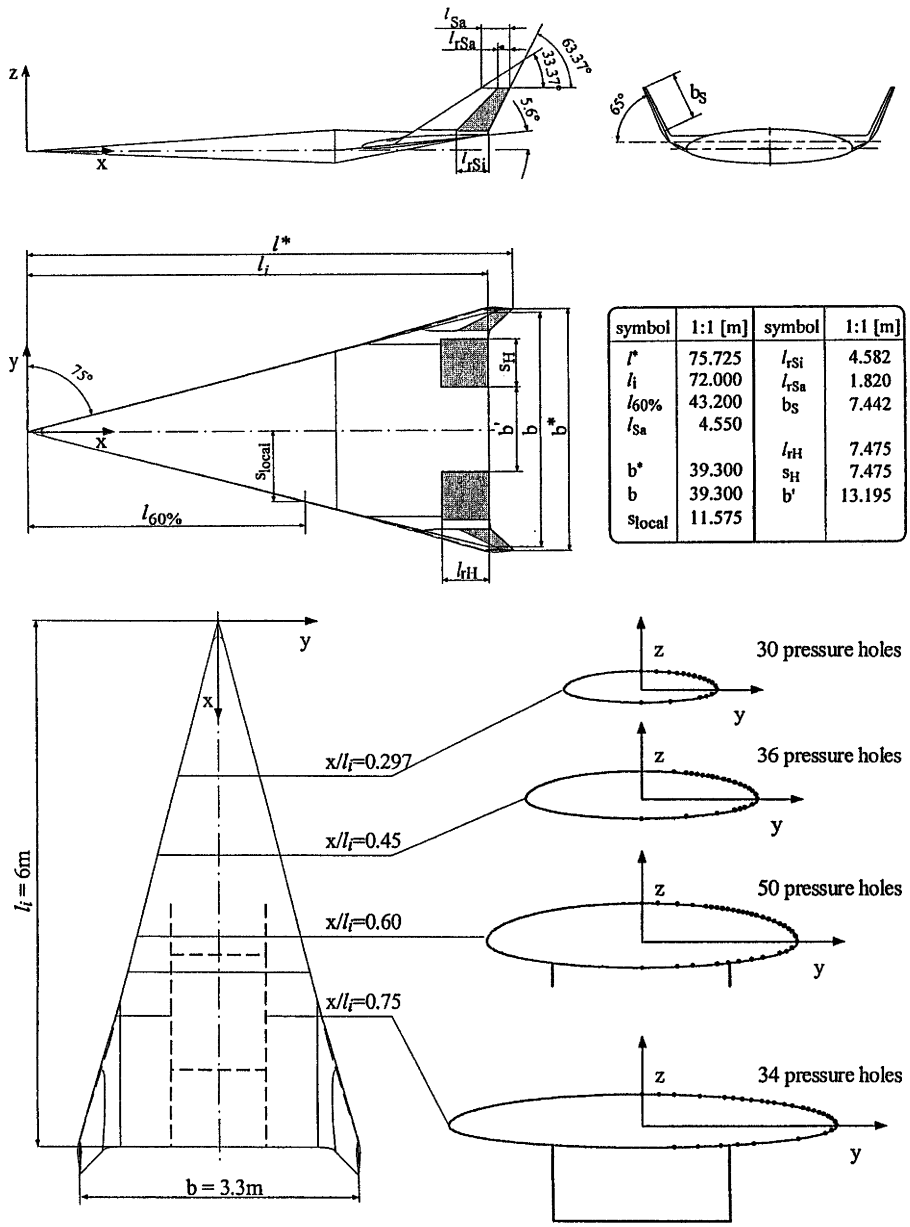

Figure 1. Geometry of the ELAC 1 configuration; model for the third DNW experiment.

Surface pressures could be measured in 4 cross sections at $x/l = 0.3, 0.45, 0.6$, and 0.75 in altogether 150 holes, and the angle of attack α could be varied over 30°, i.e. $-6° \leqslant \alpha \leqslant 24°$, and the angle of side slip over 16°, i.e. $-12° \leqslant \beta \leqslant 8°$.

Profiles of the mean velocity were measured in the boundary layer at four positions in the plane of symmetry on the leeward side of the model at $x/l = 0.125, 0.25, 0.375$, and 0.625. The four measuring positions are indicated in *figure 2*.

For detection of transition and separation the model was instrumented with three multi-sensor hot film arrays at the three cross sections, indicated in *figure 3* at $x/L = 0.19, 0.37$, and 0.576. The arrays were arranged in such a way as to include the expected velocity vector within the angular range of the sensors.

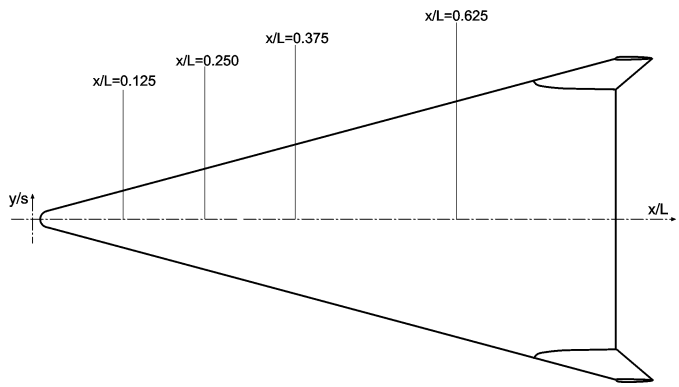

Figure 2. Positions of the boundary-layer measurements in the plane of symmetry on the leeward side of the model.

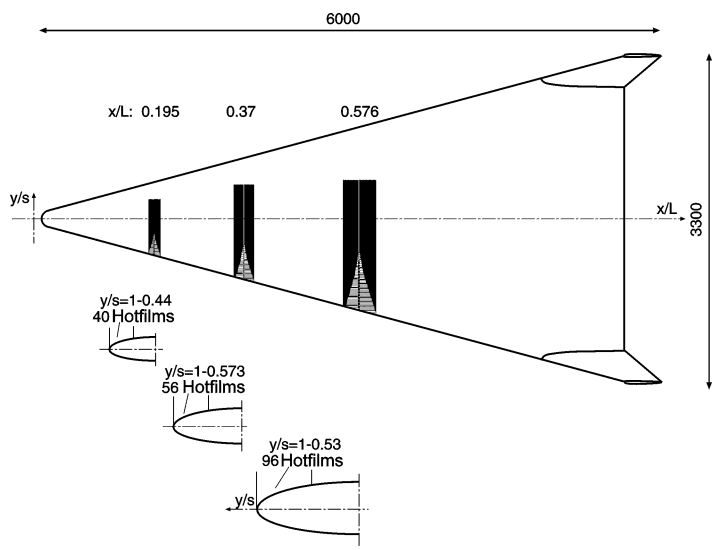

Figure 3. Positions of the hot-film measurements for detection of transition.

2.2. Experimental techniques

Because of the relatively small boundary-layer thickness at the measurement positions, the velocity measurements were carried out with a single hot wire probe. The probe was mounted on a traverse mechanism, specially designed for the experiment. It could be moved from a minimum distance of 0.2 mm from the surface of the model up to 100 mm in the direction normal to the surface. Measurements were obtained at the four positions $x/l = 0.125, 0.25, 0.375$ and 0.625 in the center chord.

The hot-wire instrumentation consisted of a TSI IFA 100 hot-wire bridge. The signals were digitized with an AD-card and the statistical moments were calculated on an IBM compatible PC. Altogether 32 000 samples were taken with a frequency of 10 kHz.

The hot-wire probes were built at the Aerodynamisches Institut Aachen. The probe dimensions were as follows: The diameter of the wire was $d = 5.0.\ \mu$m, its length $l = 2.0$ mm, and the effective length $l_{\text{act}} = 1.0$ mm. The wire was gold plated at the ends. The probe was calibrated in situ against the static pressure of the settling chamber upstream of the nozzle.

In total 4 hours were available for setting up and testing the measuring equipment, with an additional half an hour for repositioning the probe from one measuring position to the others, and 8 hours for performing the actual measurements.

Originally, skin friction measurements with a Preston tube were also proposed for the same positions where the hot wire measurements were carried out. Due to the local curvature of the surface, the static pressure could not be measured through holes drilled in the wall near the location of the Preston tube. But even a special Preston tube, designed by I. Rechenberg [9], which also measured the total pressure at the same position where the static pressure was obtained, gave wrong results for the position farthest upstream and at large angles of attack. For that reason, the data obtained with the Preston tube were not used for the computation of the friction velocity. Since the pressure did not show variations at the measuring positions for the presented angles of attack of $0° \leqslant \alpha \leqslant 10°$, the semi-empirical relation of H.H. Fernholz was used [10]. That relation is obtained by integrating the momentum equation across the viscous sublayer, the layer in which the universal law of the wall is valid, and across the outer part of the boundary layer, where the defect law is valid. Thereby the friction velocity can be expressed in terms of the external velocity U_∞, and for incompressible flow the following formula is obtained for $\mathrm{Re}_{\delta 2} \geqslant 2000$:

$$\frac{u_\tau}{u_\infty} = 2\left\{\left(1 - \frac{u_1}{u_\delta}\right)\left[\left(\frac{1}{\kappa} - 4.70\right)\ln\left(\frac{y}{\Delta}\right)_P - 6.74 - \frac{1}{\kappa}\ln\left(\frac{y_1}{\Delta}\right)\right]^{-1}\right\}.$$

In the above relation the quantity Δ is the Rotta–Clauser length, which is defined as

$$\Delta = \int_0^\delta \frac{u_\delta - \overline{u}}{u_\tau}\,\mathrm{d}y$$

and the natural logarithm of the ratio $(y/\Delta)_P$ can according to [10], be expressed by the following relation:

$$\ln\left(\frac{y}{\Delta}\right)_P = -0.404\,\mathrm{Re}_{\delta 2} + 0.37.$$

These relations were used in the following to determine the friction velocity u_τ. The subscript p indicates the point in the boundary layer, where the universal law of the wall is matched with the defect law for the outer region; the coordinate y_1 is the boundary between the viscous sublayer and the region in which the universal law of the wall is valid.

For detection of transition and separation the model of the ELAC l configuration was instrumented with three multi-sensor hot film arrays equipped with 40, 56 and 96 hot film elements at three cross sections ($x/l = 0.19, 0.37$ and 0.576) on the leeward side of the model near the leading edge, see *figure 3*. Each sensor consisted of a 0.2 μm nickel film, with a length of 2.0 mm, and a width of 0.08 mm, and 2 μm copper-coated nickel leads. The sensors were spaced in a straight line at 9 mm intervals in the vicinity of the leading edge, and at 15 mm intervals away from the leading edge, covering a spanwise range of $y/s = 0.5$ to $y/s = 1.0$.

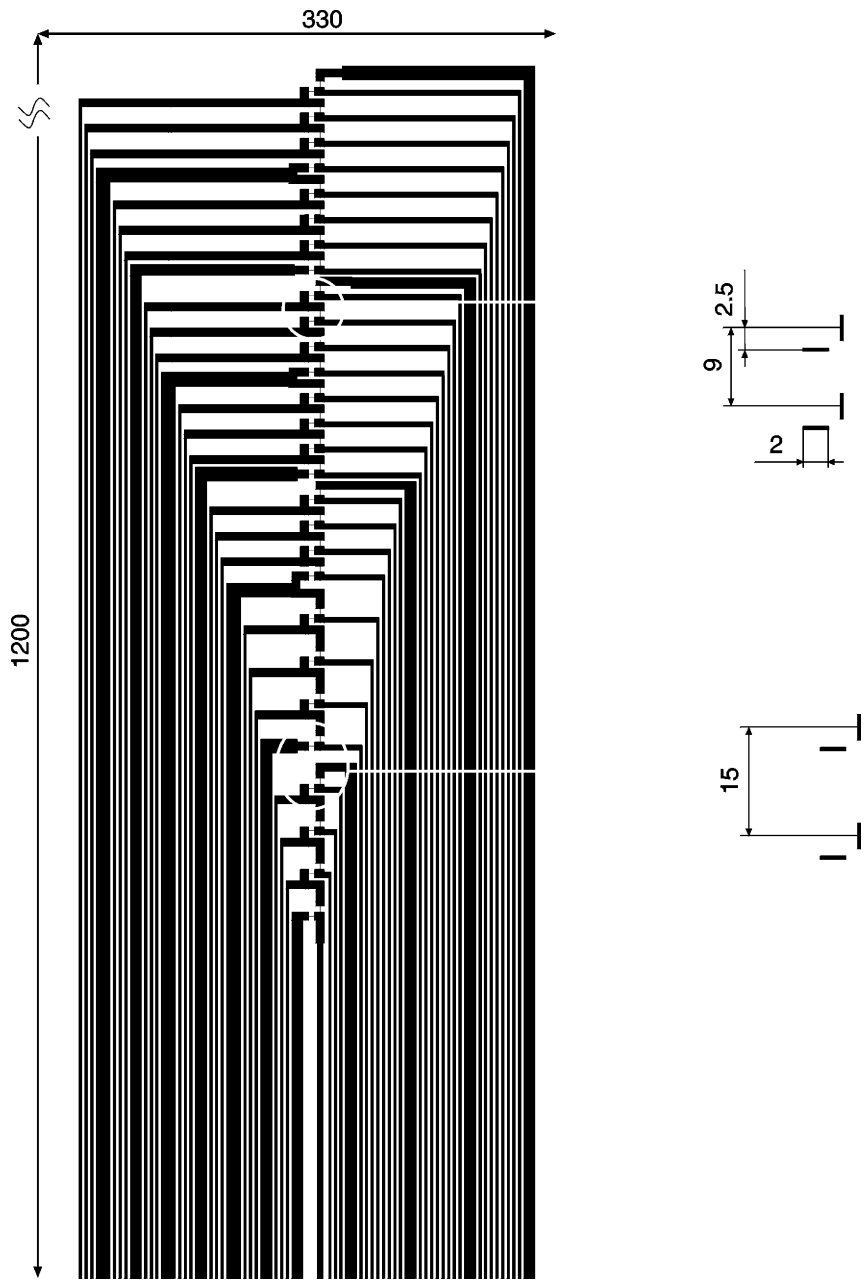

Figure 4. Arrangement of hot-film elements in multi-sensor array (top view).

The non-calibrated hot film elements were operated with a multi-channel constant-current anemometer, with which 96 probes could be operated simultaneously. Eight sensors were connected in series and heated by a constant-current source, and only 108 leads conductors were needed for 96 sensors. The heating current could be adjusted separately for 12 groups of 8 sensor elements from 0 to 100 mA in steps of 0.5 mA. Each sensor voltage was amplified by automatically offset-compensated differential amplifiers. The relative amplitude decay was estimated to be 8 dB per octave in the kHz range. Frequencies up to 3 kHz could be resolved, which was sufficient for the detection of transition and separation. The anemometer system was completely computer controlled. The sensor signals were recorded simultaneously by a transient recorder with 96 channels. The measuring time was 1.6 s with a sample rate of 10 kHz.

The multi-sensor hot film arrays were also fabricated at the Aerodynamisches Institut. The lay-out of the probe with 96 elements is depicted in *figure 4*. The probe covered an area of 1200×330 mm^2 and had a thickness of 0.05 mm. The 96 single hot films are arranged in a straight line, with the double sensors forming an angle of 90°. The substrate of the foil is polyimide, coated with nickel (thickness 0.2 μm) and copper (thickness 2 μm) via sputtering. The copper reduces the electrical resistance of the leads. The pattern of the array was generated with a differential-etching technique. The sensor foil has a maximum roughness height of 2.2 μm. For further details see M. Kornberger [11].

3. Numerical integration of the boundary-layer equations

In order to be able to compare the experimental data with results of boundary-layer calculations, a numerical solution of the boundary-layer equations for compressible, three-dimensional, turbulent flow was employed to recompute the velocity profiles at the measuring positions. The solution was described by V.N. Vetlutsky and the first author in detail in [12], and only a short summarizing description is given here. For the solution of the boundary-layer equations in three dimensions, it is necessary to describe the surface of the body. It proved to be convenient to assume, that the body has a longitudinal axis coinciding with the x-axis. Then the surface of the body can be described by cylindrical coordinates $r = r(x, \theta)$, where θ is the meridional angle in every cross section. The origin of the coordinates was positioned at the apex of the body, and the meridional angle $\theta = 0$ was measured from a reference plane on the windward side of the body, for example the plane of symmetry, but any other plane can be used. The boundary-layer equations are written in a non-orthogonal system of coordinates, (ξ, η, ζ), orientated with respect to the surface of the body, the two tangential coordinates being ξ and ζ, and η the coordinate in the direction of the outward normal at the point considered. The equations are written in non-dimensionalized form, with all quantities referenced to corresponding free-stream conditions and an appropriate length. To compensate for the growth of the boundary layer, the normal velocity component and the normal coordinate are stretched in the manner of similar solutions. The system is closed with temperature dependent relations for the viscosity, thermal conductivity, and the specific heat at constant pressure.

The integration can be initiated by either assuming similar profiles in the vicinity of the apex of the body or by prescribing initial conditions for the two tangential velocity components and the temperature, obtained, for example, from measurements. The boundary conditions at the wall are given by the no-slip condition and a prescribed wall temperature. The external boundary conditions may be obtained from a numerical solution of the Euler equations, or again from experimental data. The solution used here has repeatedly employed external boundary conditions generated with the numerical solution of E.M. Houtmann and W.J. Bannink for the Euler equations [13].

The solution given in [12] can also be used for the computation of transitional and turbulent boundary layers, provided suitable transition criteria and closure assumptions are available. In [12] the Michel, the

Cebeci–Smith, the Pletcher, and the Baldwin–Lomax closure models were tested and the results compared to experimental data. It could be shown, that all four models yielded almost the same results.

The difference forms of the boundary-layer equations were constructed with implicit differencing of formal second-order accuracy. The algebraic equations resulting from the discretization are linearized and solved in an iteration procedure. Variable step-size arrangement is included in the algorithm.

Despite the marked progress in the development of numerical solutions for the Navier–Stokes equations, for high-Reynolds number flows solutions of the boundary-layer equations remain attractive for non-separating flows, as they can provide finer resolution in the vicinity of the wall in comparison to numerical solutions of the Navier–Stokes equations and can thereby provide more accurate prediction of the skin friction and the heat transfer. This point of view is confirmed by recent publications on the subject, most of them giving wall pressure distributions but not skin friction and heat transfer.

4. Discussion of experimental results

The hot-wire measurements were carried out in the plane of symmetry ($y = 0$) at a free-stream velocity of $U_\infty = 50$ m/s with the single-wire probe described earlier. The results obtained at the four measuring positions are given for the angles of attack $\alpha = 0°, 6°$, and $12°$ in *figure 5*. The velocity profiles for $\alpha = 6°$ seem to exhibit the natural development of the boundary layer. For $\alpha = 0°$, data was lost for the position farthest downstream at $x/l = 0.625$. For $\alpha = 12°$, the profile at the position farthest upstream, at $x/l = 0.125$, intersects the profile measured at $x/l = 0.250$; a plausible explanation could be that, with increased angle of attack, the flow begins to suffer from the influence of cross flow.

The measurements with the Preston tube were included in the tests in order to be able to study the flow behavior in the frame of inner-law scaling. Unfortunately, the results seemed to contain irregularities that

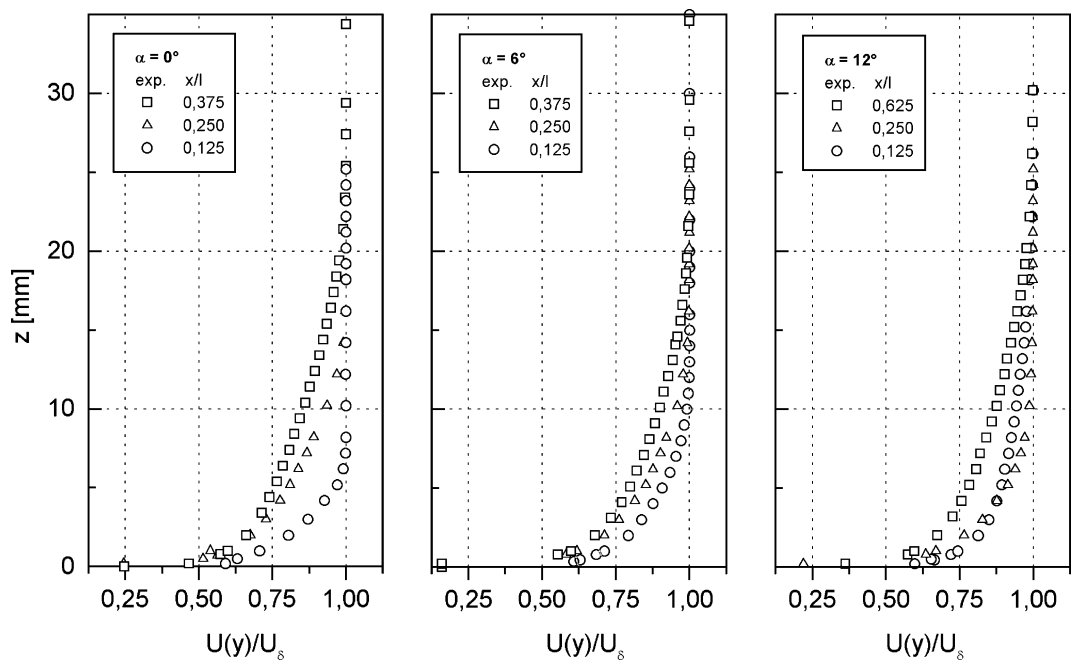

Figure 5. Measured mean velocity profiles for three angles of attack; $U_\infty = 50$ m/s.

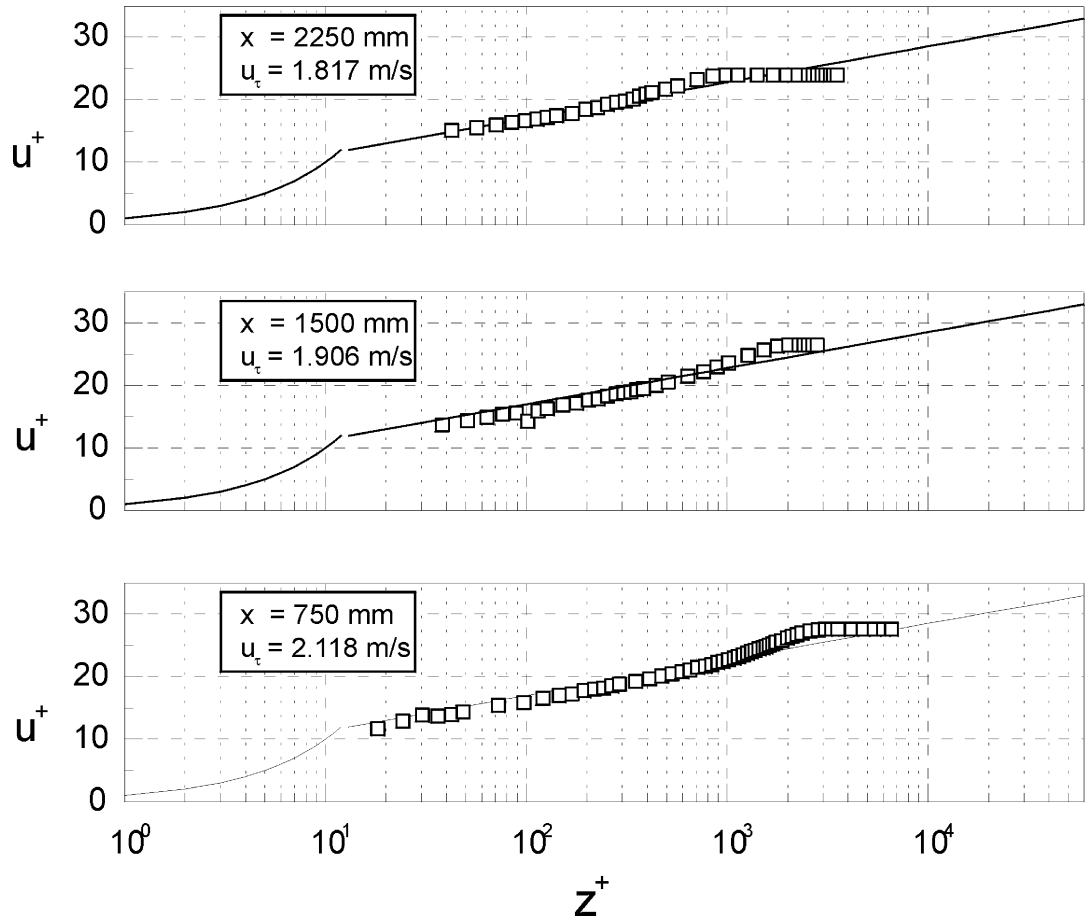

Figure 6. Mean velocity profiles plotted in inner-law scaling, $U_\infty = 50$ m/s, $\alpha = 0°$.

could not be explained. As it was known from previous pressure measurements, that the pressure gradient in the direction of the main stream was negligibly small over the distance where the velocity profiles were measured, the semi-empirical relation for the friction velocity u_τ as derived by H.H. Fernholz in [10] was used instead of the results expected from the measurements with the Preston tube. *Figures 6*, *7*, and *8* show the nondimensionalized velocities plotted versus the dimensionless coordinate z^+.

It is seen that the measured data follow the universal law of the wall, in which the constants $\kappa = 0.40$ and $C = 5.1$ were used. The deviations of the experimental data from the universal law of the wall are small over the major part of the boundary layer, indicating that the influence of the cross-flow on the main flow, represented by u^+, at the angles of attack at which these measurements were obtained, is difficult to detect in *Figures 6*, *7* and *8*.

Figure 9 shows the comparison of the experimentally determined velocity profiles, now plotted versus the normal coordinate, with the numerical results. The latter were obtained with the two-dimensional version of the numerical solution for the boundary-layer equations. The version for three-dimensional flow could not be used, as in the experiments the outer boundary conditions, necessary for the integration, could only be determined along certain lines, but not for the entire surface of the body. Using the numerical results for two-dimensional flow offers the advantage that the influence of the cross-flow can be detected by comparing the numerical

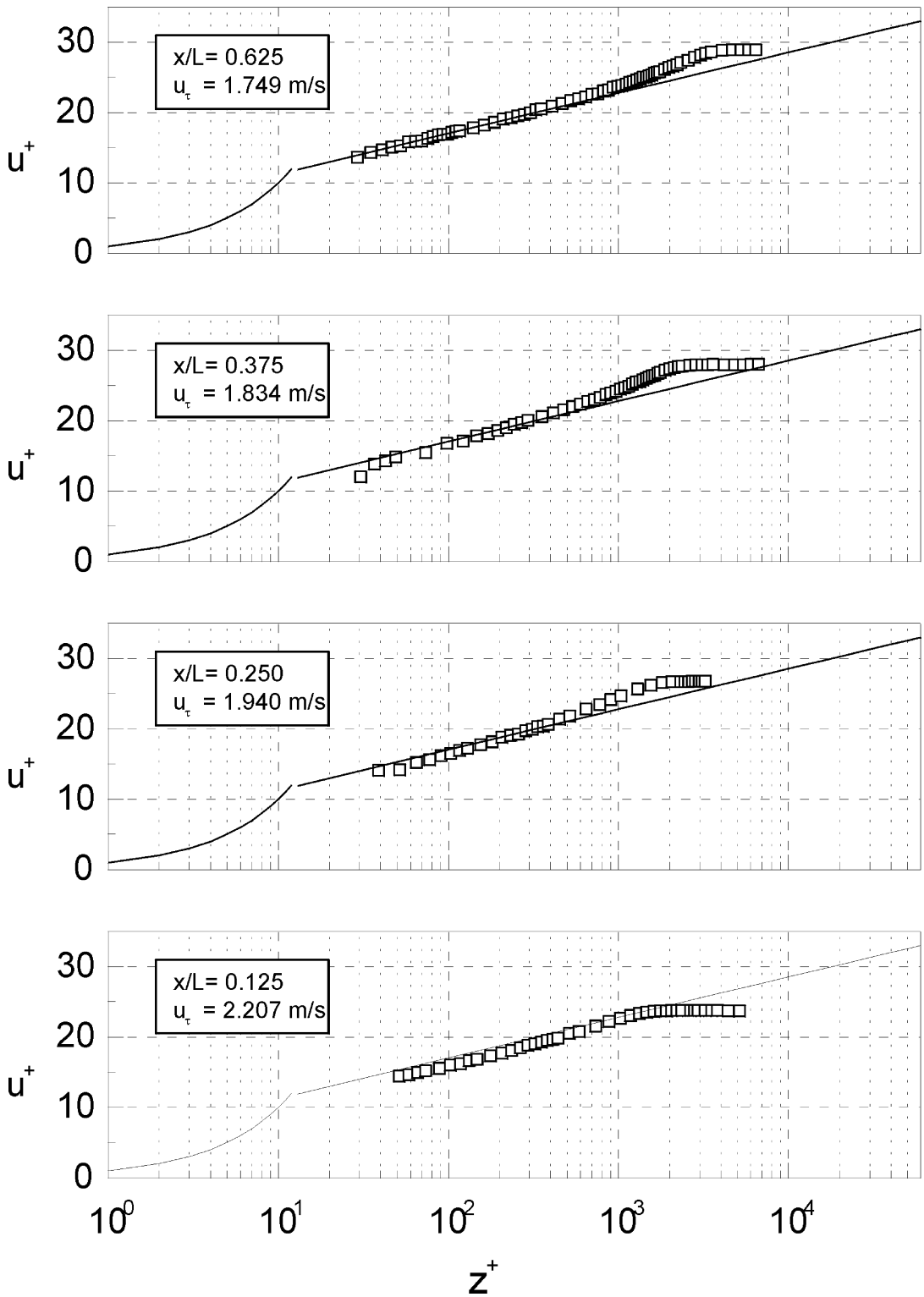

Figure 7. Mean velocity profiles plotted in inner-law scaling, $U_\infty = 50$ m/s, $\alpha = 6°$.

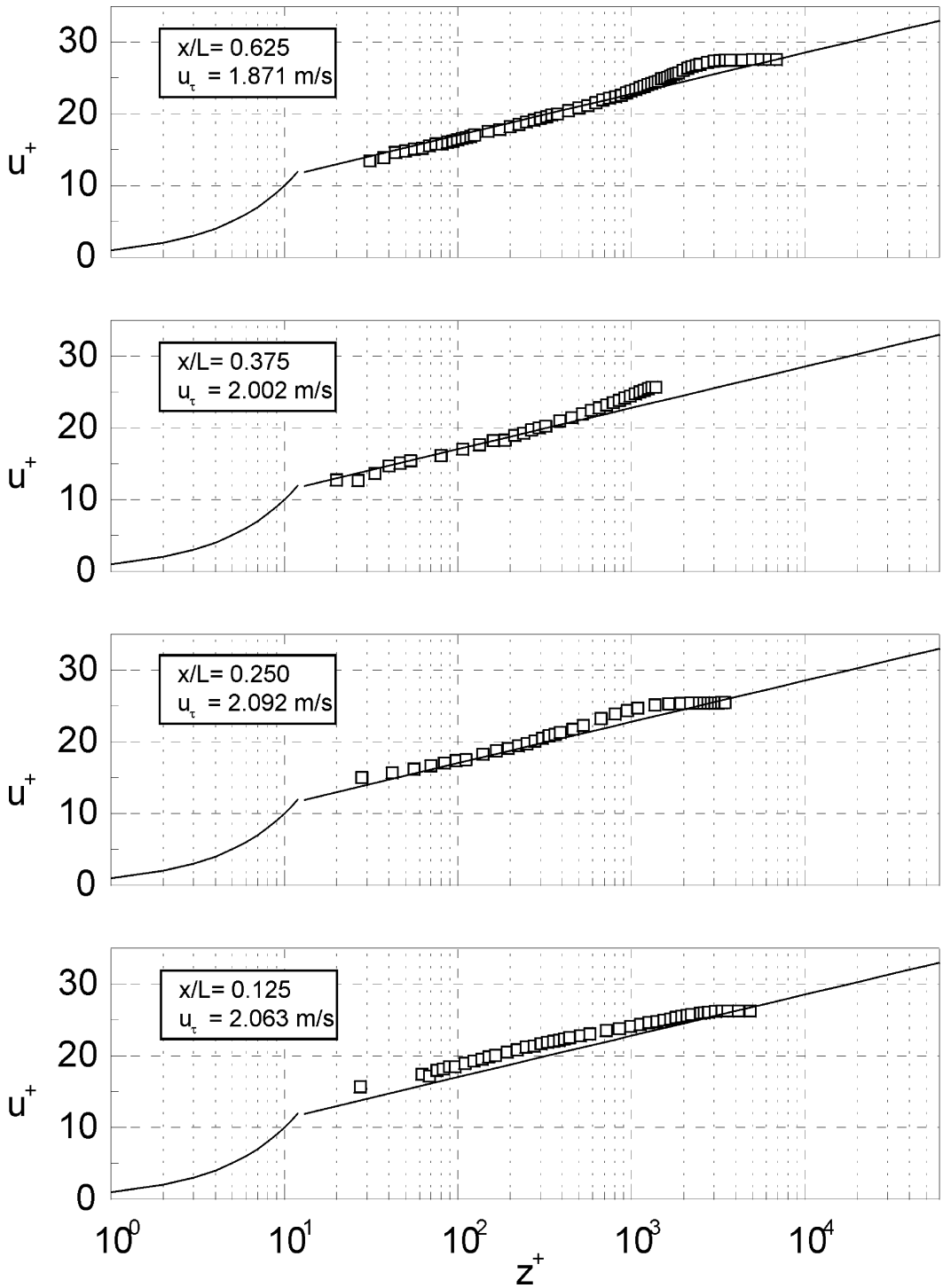

Figure 8. Mean velocity profiles plotted in inner-law scaling, $U_\infty = 50$ m/s, $\alpha = 12°$.

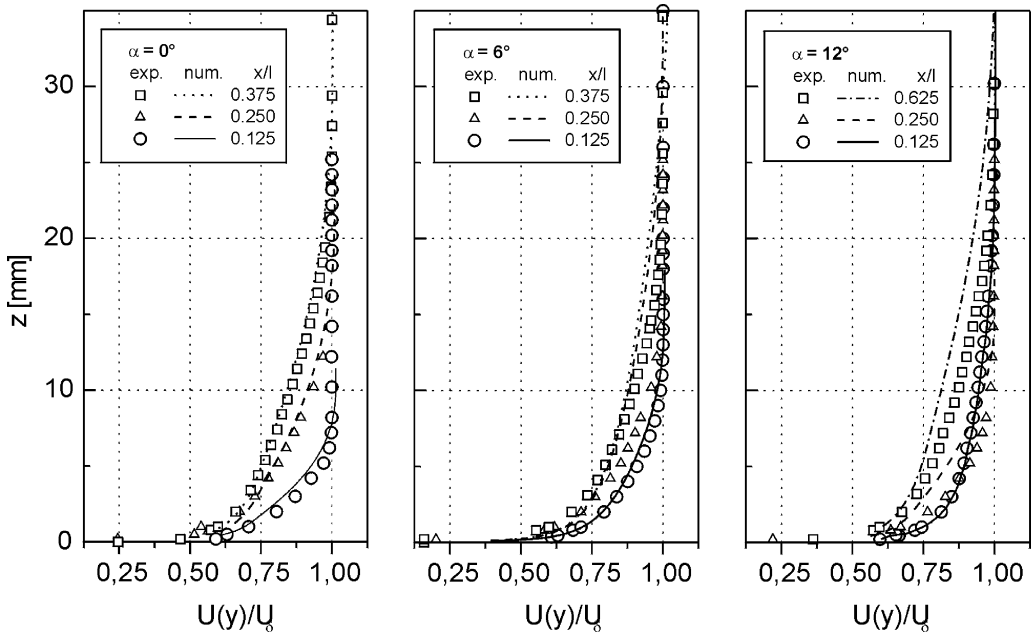

Figure 9. Measured mean velocity profiles compared to numerically calculated profiles for different angles of attack and streamwise positions; $U_\infty = 50$ m/s.

data with the experimental results. For the calculation the entire flow in the plane of symmetry was assumed to be turbulent. The Baldwin–Lomax model was used for closure. The integration was initiated by using the experimentally determined velocity profiles at $x/l = 0.125$ as initial conditions. The comparison shows, that for the angle of attack $\alpha = 0°$, the agreement between measured and computed data is good for $x/l = 0.250$ and 0.375, indicating that the influence of the cross-flow on the velocity profiles is small. For $\alpha = 6°$, and even more so for $\alpha = 12°$, the computed values deviate substantially from the measurements, particularly in the outer part of the boundary layer. Provided that the closure assumptions used correctly describe the Reynolds stresses, the deviation between the experiment and the computation must be attributed to the influence of the cross flow on the experimental results on the leeward side of the wing. On the whole, the comparison with the experimental data shows that, for angles of attack $\alpha \leqslant 9°$, the deviations between experimental and numerical results are relatively small. A noticeable influence of the cross-flow seems to set in at angles of attack $\alpha > 9°$. This value roughly coincides with the onset of formation of the primary vortex on the leeward side of the wing.

Skin friction coefficients as computed with the numerical solution of the boundary-layer equations of [12] for two-dimensional flow with data obtained from the semi-empirical relation of H.H. Fernholz of [10], in which measured values were inserted, are shown in *figure 10*. The numerical data consist out of two sets. The first set is obtained in the computation in which the measured velocity profiles at $x/l = 0.125$ were used as initial data. The skin-friction values so computed for $\alpha = 0°, 6°$, and $12°$ all fall within the shaded area in *figure 10*. The symbols give the values computed from the experimental data with the method of H.H. Fernholz [10]. For $\alpha = 0°$, and $\alpha = 6°$ the measured data are in close agreement with the computed values, but large differences are noted for $\alpha = 12°$, obviously caused by the cross-flow, as mentioned before. The second set of computed skin-friction coefficients is obtained for initial conditions prescribed at $x/l = 0.05$. They were generated with a similar solution for laminar flow, which then was forced to transition to turbulent flow over a short distance. The computed values of the skin friction are shown by the solid line ($\alpha = 0°$), the dashed line ($\alpha = 6°$), and the dashed dotted line ($\alpha = 12°$). These data differ from the first set only in the vicinity of the initial region,

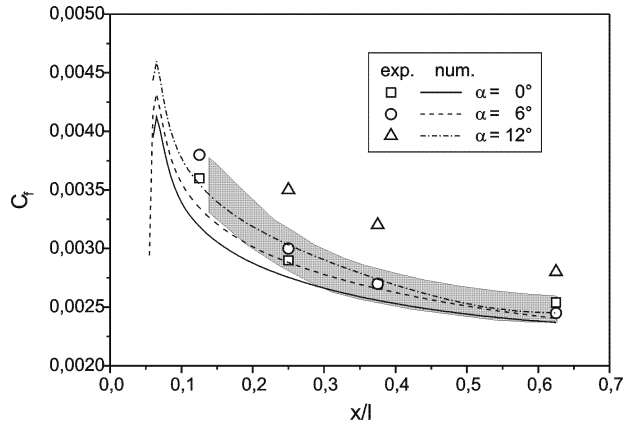

Figure 10. Comparison of skin friction coefficients as computed with the numerical solution of [12] and the semi-empirical relation of [10]; $U_\infty = 50$ m/s.

further downstream they coincide with the first set and the experimental data for $\alpha = 0°$, and $\alpha = 6°$. Again, for small angles of attack, the influence of the cross-flow is negligible, while for $\alpha = 12°$ there is a large difference between measured and computed data, indicating that a noticeable amount of cross-flow was initiated by the increase in angle of attack.

5. Studies of transition and separation

Transition measurements were performed for free-stream velocities varying from $U_\infty = 30$ m/s to $U_\infty = 90$ m/s at zero angle of sideslip ($\beta = 0$). In the tests, the angle of attack was varied between $-3° \leqslant \alpha \leqslant 24°$. An additional test was performed with an angle of sideslip ($\beta = -12°$) at a free-stream velocity of $U_\infty = 70$ m/s. The hot-film elements yield typical time traces for laminar, transitional, and turbulent flow. Laminar flow is indicated by signals with negligible amplitudes. The onset of transition is characterized by fluctuations with drastically increased amplitudes, whereas fully developed turbulent flow again exhibits different fluctuation characteristics. The differences in the time traces for laminar, transitional and turbulent flow are particularly evident for the lower frequencies, e.g., $f < 1000$ Hz, as shown in *figure 11*, where typical power spectra

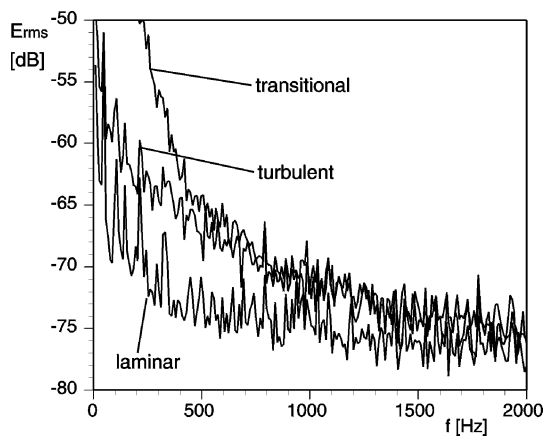

Figure 11. Typical power spectra of hot-film signals for laminar, transitional, and turbulent flow.

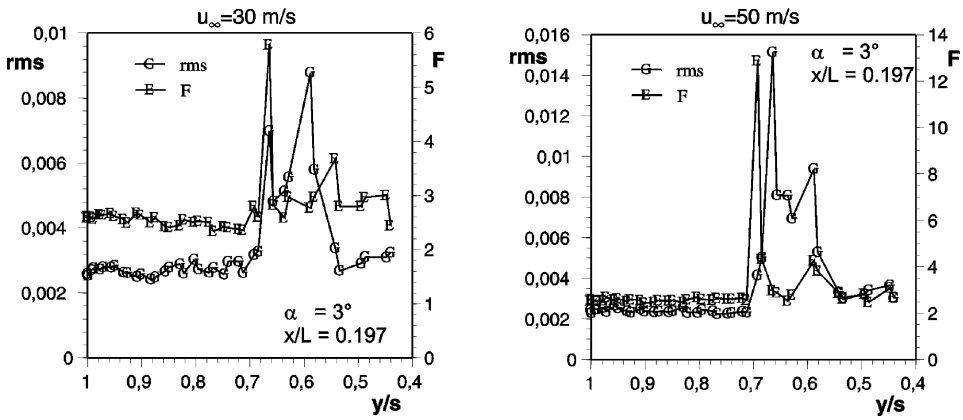

Figure 12. Rms-values and flatness F of the sensor signals for an angle of attack $\alpha = 3°$ and $x/l = 0.195$.

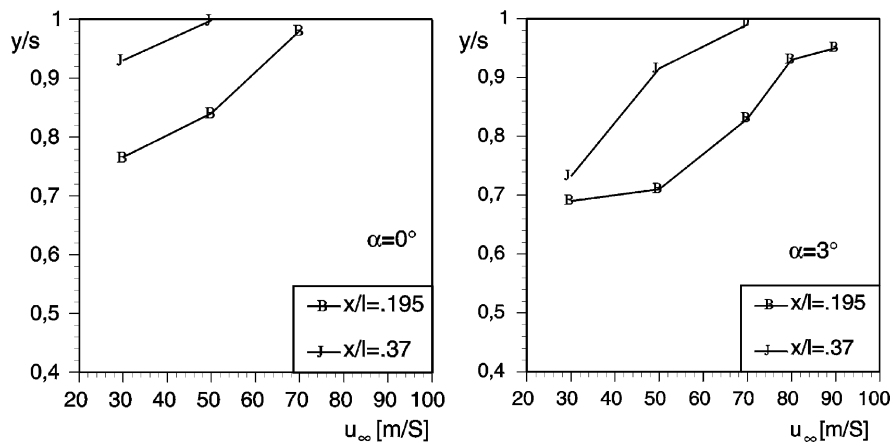

Figure 13. Location of transition as determined with the multi-sensor hot-film technique for $\alpha = 0°$ and $\alpha = 3°$ and different free-stream velocities, from diagrams as depicted in *figure 12*; for details see text.

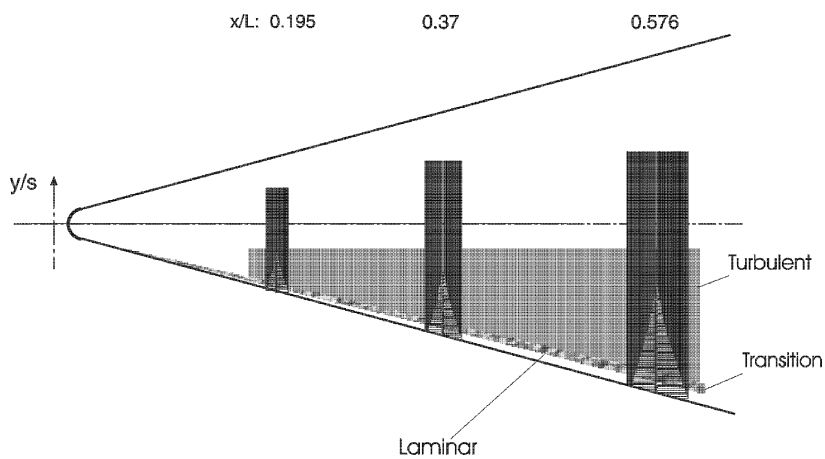

Figure 14. Geometry of the ELAC 1 configuration; model with the areas of the laminar and turbulent flow and the region of transition for $\alpha = 9°$ and $U_\infty = 70$ m/s.

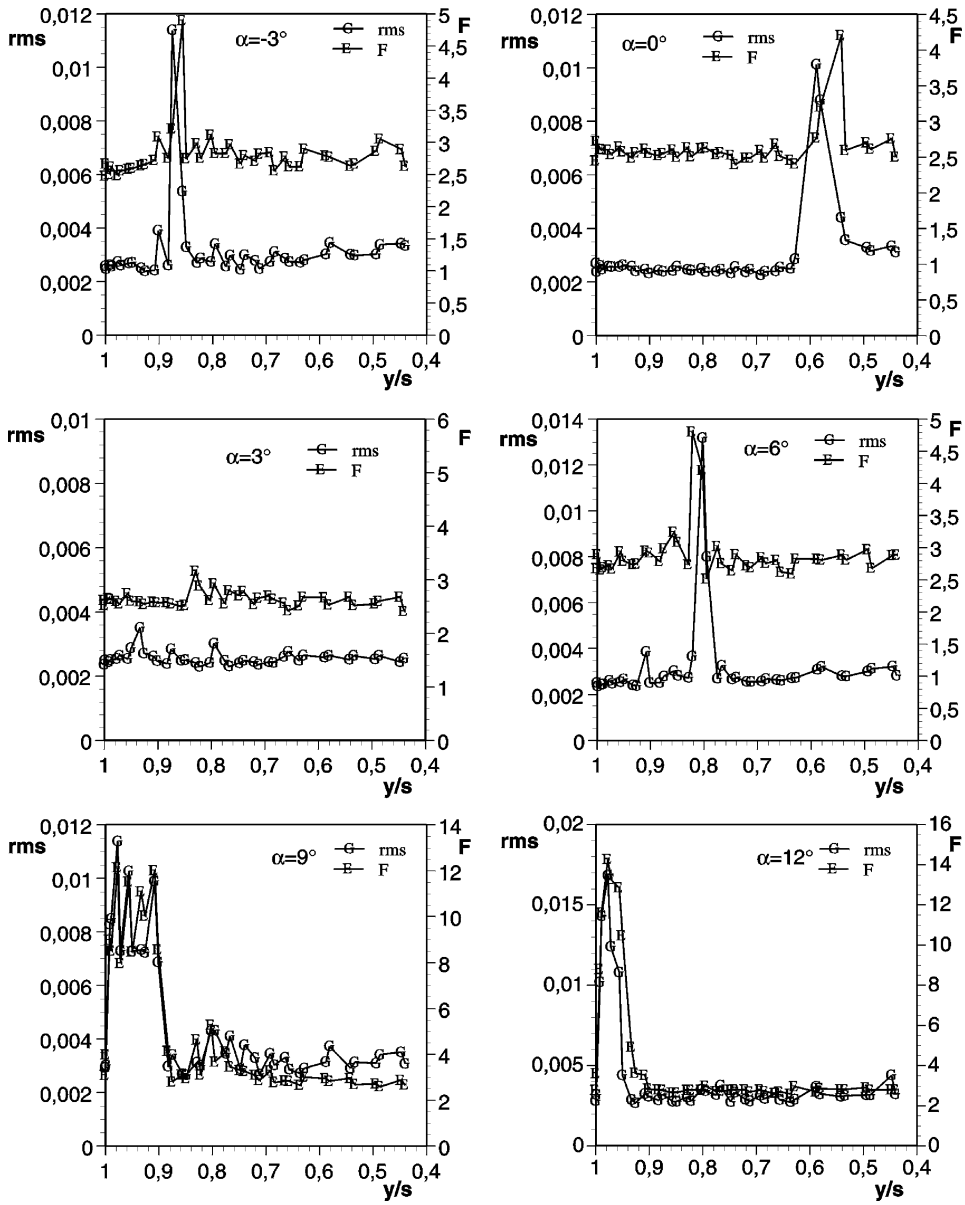

Figure 15. Rms-values and flatness F of the sensor signals for different angles of attack and an angle of sideslip $\beta = -12°$, $x/l = 0.19$; $U_\infty = 70$ m/s.

are depicted. Because of the distinct differences in the signals, transition can be detected by determining the standard deviation (rms-values) and moments of higher order (flatness F) computed from the time traces [11]. Details of such studies may be found in [14], where detection of transition was demonstrated for the flow over a wing in free-flight experiments.

In the investigation described here the onset of transition was determined in the same manner as described in [14]. For the detection oft the transition the flatness F is used instead of the time traces. This quantity is to be preferred since in the transition region the flatness F is always larger than 3. In *figure 12*, the rms-values and the flatness F are plotted versus the dimensionless spanwise coordinate y/s for free-stream velocities $U_\infty = 30$ m/s

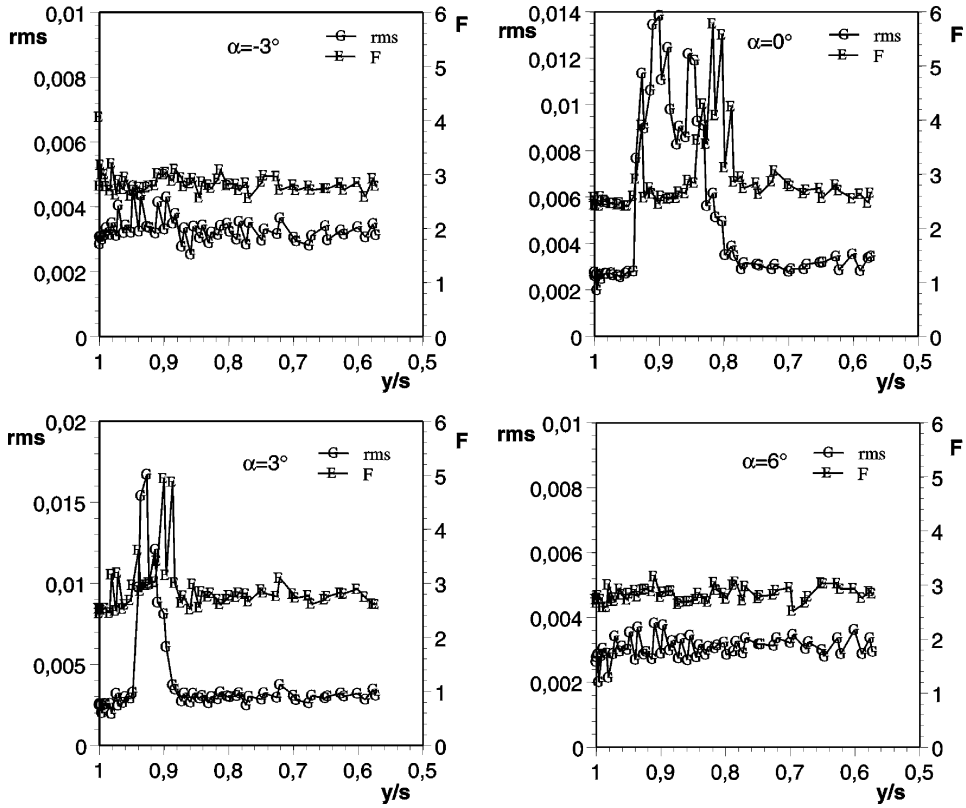

Figure 16. Rms-values and flatness F of the sensor signals for different angles of attack and an angle of sideslip $\beta = -12°$, $x/l = 0.37$; $U_\infty = 70$ m/s.

(left diagram) and $U_\infty = 50$ m/s (right diagram) for a value of $x/l = 0.197$ and for an angle of attack $\alpha = 3°$. The rms-values and the flatness F show clearly distinguishable peaks, both closely together, indicating the region of transition for $U_\infty = 30$ m/s at about $y/s \approx 0.6 - 0.7$ and for $U_\infty = 60$ m/s at $y/s \approx 0.7$. Such diagrams can be constructed for all test velocities and the location of transition so determined can be shown as a function of the free-stream velocity, as for example for the first two measuring positions $x/l = 0.195$ and 0.37 in the diagrams shown in *figure 13*. It is seen that the flow becomes turbulent in the immediate vicinity of the leading edge. *Figure 14* indicates that transition ocurs in a narrow strip, almost parallel to the leading edge.

For larger angles of attack and angles of sideslip, the flow becomes turbulent even closer to the leading edge. This can be seen in *figure 15* for $x/l = 0.19$ and in *figure 16* for $x/l = 0.37$, where the rms-values and the flatness F of the sensor signals are shown for several angles of attack and the angle of sideslip $\beta = -12°$. The free-stream velocity is $U_\infty = 70$ m/s for both cases. Transition gives rise to a marked increase of the rms-values and the flatness F. For angles of attack of $-3°$ and $6°$ in *figure 16*, the location of the transition is not evident as it is for the other angles of attack. This, however, is not an indication of a lack of a transition and is more likely due to the transition being located closer to the lower surface of the leading edge, out of the range of the hot-film sensors.

In a fashion similar to the detection of transition, the multi-sensor hot-film technique can also be used to detect separation. This was pointed out already by J.P. Stack, S.M. Mangalam, and V. Kalburgi in 1988 in [15]. These authors showed, that separation is characterized by a phase reversal in low-frequency dynamic shear stress signals. This can been seen in *figure 17*, where the phase difference and the coherence of neighboring sensors upstream (9–11) and downstream (11–13) are depicted, and in *figure 18*, which shows the linear

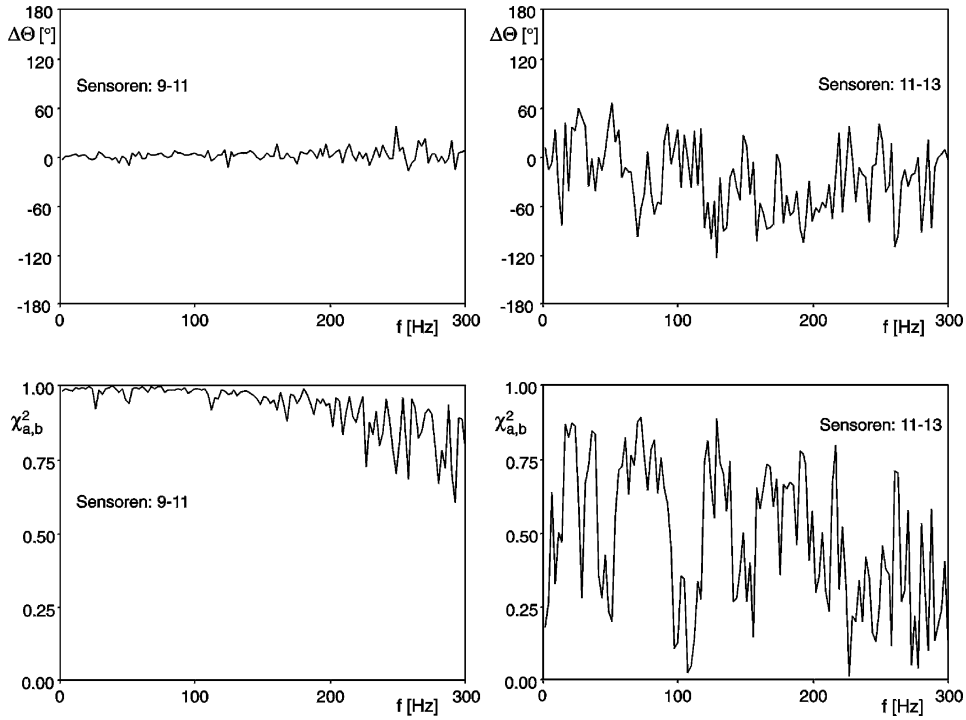

Figure 17. Phase difference $\Delta\Phi$ and coherence $X^2_{a,b}$ of signals of neighboring sensors upstream and downstream from separation.

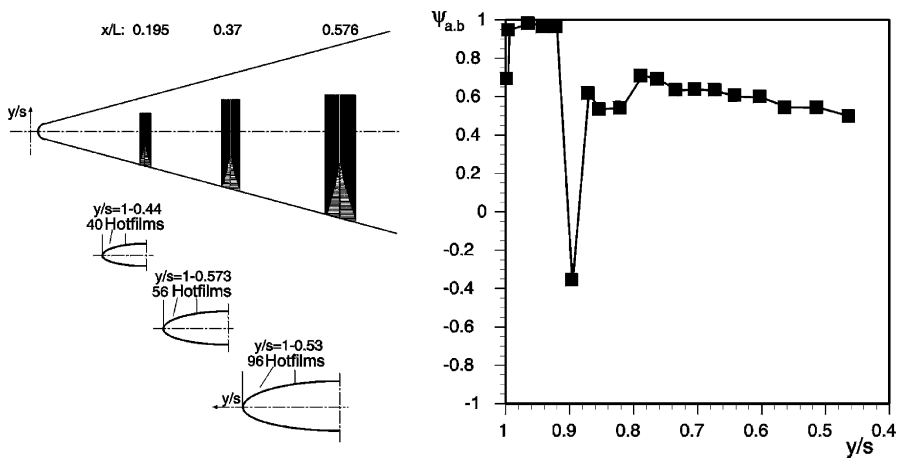

Figure 18. Correlation function $\Psi_{a,b}$ obtained with the signals of neighboring sensors, see also in *figure 4*.

correlation function ψ_{ab}, obtained from the signals of neighboring sensors. Using this technique, separation was detected in the experiments for angles of attack $\alpha \geqslant 9°$. The influence of the free-stream velocity U_∞ and the angle of attack α on the separation line of the primary vortex is shown in *figure 19*, and for the secondary vortex in *figure 20*. It can be seen that separation moves towards the line of symmetry with an increase in U_∞, whereas the influence of the angle of attack on the separation lines is less pronounced. The results obtained indicate, that the primary separation moves towards the leading edge with increasing angle of attack and increasing free-stream velocity, while the secondary separation line does not seem to correlate with the angle of attack.

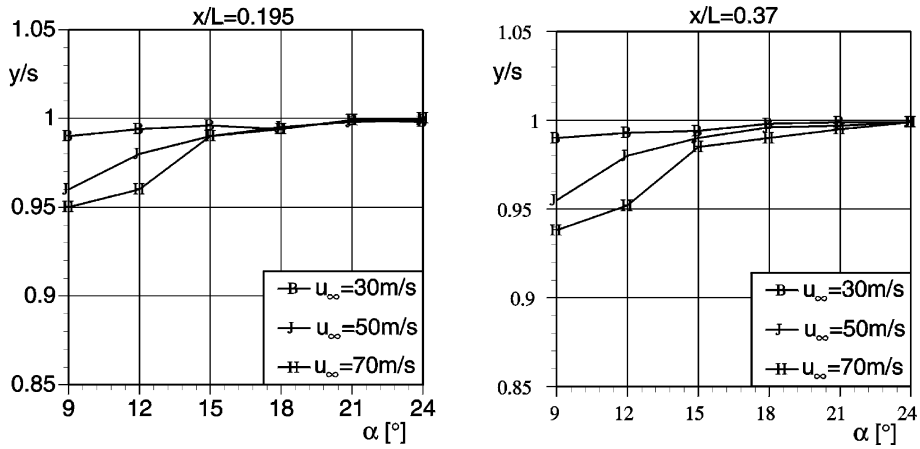

Figure 19. Separation line of the primary vortex, determined with the multi-sensor hot-wire technique.

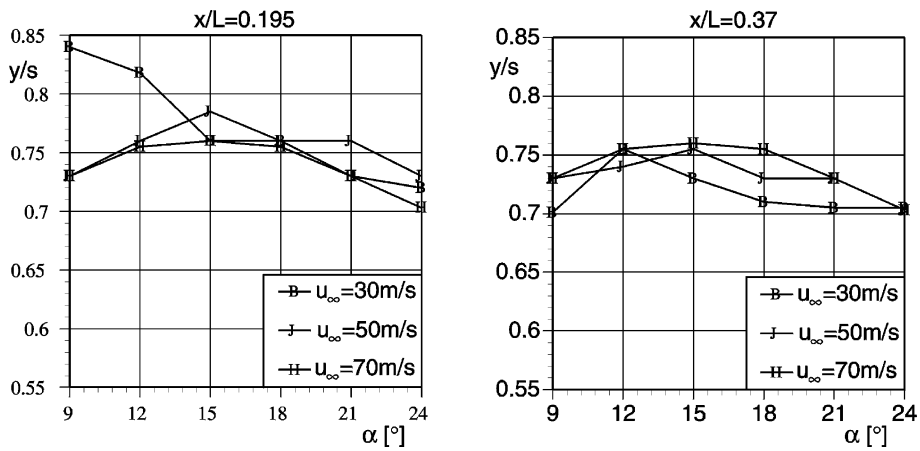

Figure 20. Separation line of the secondary vortex, determined with the multi-sensor hot-wire technique.

6. Conclusions

The boundary layer on the leeward side of a 1 : 12 scale model of the ELAC 1 configuration of a space transportation system was investigated experimentally and with numerical techniques. The experiments were carried out in the 8×6 m^2 low-speed German-Dutch-Windtunnel at Reynolds numbers up to $\mathrm{Re} = 40 \cdot 10^6$. Mean velocity profiles were determined in the turbulent boundary layer on the leeward side of the model, with a single hot-wire probe in the plane of symmetry at four positions. Comparison calculations with a numerical solution of the boundary-layer equations showed good agreement up to angles of attack $\alpha = 10°$. The laminar-turbulent transition of the flow and its separation near the rounded leading edge were investigated at three positions with multi-sensor hot-film arrays. These measurements showed that transition and separation can safely be detected with the hot-film technique. The results clearly indicate that the flow near a rounded leading edge is markedly influenced by the magnitude of the nose radius.

The results obtained in the third DNW experiment confirm that model and measuring techniques have sufficiently matured so that large-scale experiments can provide reliable experimental data for high-Reynolds number flows.

Acknowledgements

The authors gratefully the continuous support of their work by the DFG. They also acknowledge the support offered by Prof. Dr.-Ing. H.U. Meier, the former director of the DNW, and his team.

References

[1] Fernholz H.H., Krause E., Nockemann M., Schober M., Comparative measurements in the canonical boundary layer at $Re_{\delta_2} \leqslant 6 \times 10^4$ on the wall of the German-Dutch windtunnel, Phys. Fluid 7 (1995) 1275–1281.
[2] Rotta J.C., Meier H.U., Private Communication, Göttingen, 1996.
[3] Kreplin H.-P., Merschat O., Abstiens R., Korrelationsmessungen in der Wandgrenzschicht des Deutsch-Niederländischen Windkanals (DNW), DGLR-Fach-Symposium der AG-STAB, Berlin, 10.–12.11.1998.
[4] Jacob D., Neuwerth G., Peiter U., High Reynolds number wind tunnel tests with an ELAC-model in the DNW, in: Krause E. (Ed.), Special Issue 'Space Transportation Systems', GAMM Annual Meeting 1998, Bremen, April 6–9, 1998, pp. 57–60.
[5] Neuwerth G., Peiter U., Decker F., Jacob D., Reynolds Number Effects on the Low-Speed Aerodynamics of the Hypersonic Configuration ELAC 1, AIAA-98–1578, April 1998.
[6] Abstiens R., Fühling S., Vetlutsky V.N., Boundary-layer measurements on the ELAC 1 configuration at $Re = 4 \times 10^7$, in: Krause E. (Ed.), Special Issue 'Space Transportation Systems', GAMM Annual Meeting 1998, Bremen, April 6–9, 1998, pp. 61–62.
[7] Dieterle L., Peiter U., ELAC 1: Experimental investigation of vortex structures using PIV, in: Krause E. (Ed.), Special Issue 'Space Transportation Systems', GAMM Annual Meeting 1998, Bremen, April 6–9, 1998, pp. 63–64.
[8] Meier H.U., Michel U., Kreplin H.P., The influence of wind tunnel turbulence on the boundary layer transition, in: Meier H.U., Bradshaw P. (Eds.), Perspectives in Turbulence Studies, Springer-Verlag, 1987, pp. 26–46.
[9] Rechenberg I., Zur Messung der turbulenten Wandreibung mit dem Prestonrohr, Jahrbuch der WGLR, S. 151, 1962.
[10] Fernholz H.H., Ein halbempirisches Gesetz für die Wandreibung in kompressiblen turbulenten Grenzschichten bei isothermer und adiabater Wand, ZAMM 51 (1971) 146–147.
[11] Kornberger M., Multisensor-Heißfilmtechnik zur Transitionserkennung im Windkanal and Freiflug, Diss. RWTH Aachen, Shaker Verlag Aachen – Reihe Maschinenbau, 1992.
[12] Vetlutsky V.N., Krause E., Calculation of three-dimensional, compressible boundary layer on pointed bodies and comparison with experiments, Z. Flugwiss. Weltraumforsch. (1992) 308–316.
[13] Houtmann E.M., Bannink W.J., Experimental and numerical investigation of the vortex flow over a delta wing at transonic speed. Vortex Flow Aerodynamics. AGARD CP-494, Paper 5, 1991.
[14] Ewald B., Durst F., Krause E., Nitsche W., In-flight measuring techniques for laminar flow wing development, Z. Flugwiss. Weltraumforsch. 17 (1993) 294–310.
[15] Stack J.P., Mangala S.M., Kalburgi V., The phase reversal phenomenon at flow separation and reattachment, AIAA Paper No. 88-0408, 1988.